Long optical cavities for open-path monitoring of atmospheric trace gases and aerosol extinction

Ravi M. Varma,[1,2,3] Dean S. Venables,[2,3] Albert A. Ruth,[1,3,*] Uwe Heitmann,[1] Eric Schlosser,[4] and Sophie Dixneuf[1]

[1]Department of Physics, University College Cork, Cork, Ireland

[2]Department of Chemistry, University College Cork, Cork, Ireland

[3]Environmental Research Institute, Cork, Ireland

[4]Forschungszentrum Jülich, ICG-2: Troposphäre, D-52425 Jülich, Germany

*Corresponding author: a.ruth@ucc.ie

Received 1 August 2008; revised 29 October 2008; accepted 4 December 2008; posted 8 December 2008 (Doc. ID 99695); published 8 January 2009

An incoherent broadband cavity-enhanced absorption spectroscopy setup employing a 20 m long optical cavity is described for sensitive *in situ* measurements of light extinction between 630 and 690 nm. The setup was installed at the SAPHIR atmospheric simulation chamber during an intercomparison of instruments for nitrate (NO_3) radical detection. The long cavity was stable for the entire duration of the two week campaign. A detection limit of ~2 pptv for NO_3 in an acquisition time of 5 s was established during that time. In addition to monitoring NO_3, nitrogen dioxide (NO_2) concentrations were simultaneously retrieved and compared against concurrent measurements by a chemiluminescence detector. Some results from the campaign are presented to demonstrate the performance of the instrument in an atmosphere containing water vapor and inorganic aerosol. The spectral analysis of NO_3 and NO_2, the concentration dependence of the water absorption cross sections, and the retrieval of aerosol extinction are discussed. The first deployment of the setup in the field is also briefly described.

OCIS codes: 010.1290, 010.1120, 300.6550, 120.4640.

1. Introduction

Ultrasensitive spectroscopic absorption methods based on high finesse optical cavities are among the most promising approaches for detecting atmospheric trace species with high spatial and temporal resolution [1–3]. A variety of atmospheric trace constituents have been successfully detected in the field using laser-based cavity ringdown (CRD) spectroscopy [4–7]. Most CRD field instruments extract atmospheric samples [8–13], and only a few have employed an open-path configuration [14,15]. For instruments using gas extraction, inlet losses of the target species must be established in independent measurements [16]. If a CRD method is based on measuring the absorption at a single wavelength, retrieving the concentration of a target species requires an experimentally independent method to establish the contribution of the target species to the total extinction, for instance, through concentration variation by titration or filtering [17,18]). In CRD instruments that use several wavelengths for species identification usually a cavity length scanning capability is required to access arbitrary wavelengths, which makes monitoring multiple species experimentally more demanding, except where interfering species can be chemically or thermally converted to

0003-6935/09/04B159-13$15.00/0

the target species. Alternatively, some CRD spectroscopy setups may comprise several optical cavities at different wavelengths. In this context broadband methods [e.g., conventional multipass setups [19,20] employing differential optical absorption spectroscopy (DOAS) [21]] have the advantage that atmospheric trace species can be identified by their spectral absorption signature, and additional loss processes can be accounted for in the spectral analysis. The multiplex features of broadband methods allow several target species to be detected simultaneously. Broadband CRD methods have been known for several years [22–30] and have already been applied to atmospheric trace sensing [14,31]. A drawback of these pulsed broadband CRD setups is that they require tunable laser sources along with unconventional light detection electronics and data sampling. The complexity of the instruments has hindered their widespread adoption for field observations so far.

An alternative approach is based on dispersing and detecting the light from an incoherent broadband light source after it is transmitted by an optical cavity, so-called incoherent broadband cavity-enhanced absorption spectroscopy (IBBCEAS) [32]. This continuous-wave approach has been successfully applied in a number of laboratory and open-path chamber experiments [33–35]. In addition to the benefits of the broadband method outlined above, it is characterized by several advantageous features that are particularly relevant for field deployment: IBBCEAS combines high detection sensitivity with experimental simplicity. Carefully designed instruments are robust with good long-term mechanical and optical stability. Moreover, depending on the emission spectrum of the light source used (e.g., Xe arc lamps [32,33], inexpensive light emitting diodes [34,36,37], or novel supercontinuum light sources [38]), it is relatively easy to adapt IBBCEAS setups to different wavelength regimes simply by switching cavity mirrors.

There are, however, three limitations of this approach that will be addressed in this publication. First, despite the high brightness of some incoherent light sources, unfavorable imaging conditions cause the transmission of light through a high finesse optical cavity to be generally lower than for laser sources (with the exception of supercontinuum sources [38]). Therefore long optical cavities with modest reflectivity mirrors ($R \approx 0.99$ to 0.999) are of particular relevance for nondirectional incoherent light sources (e.g., arc lamps), since they improve the signal-to-noise ratio without loss of sensitivity. The spatial resolution of long cavities (several meters up to tens of meters) is still significantly better than that of long-path DOAS setups with typical path lengths of up to several kilometers. Hence IBBCEAS with long cavities still allows localized sources of atmospheric trace constituents to be identified. Moreover, using cavities on a scale of tens of meters is particularly suited for air quality studies of medium-sized anthropogenic pollution sources such as industrial plants, airfields, or traffic intersections.

Second, all absorption methods based on optically stable cavities (CRD and CEA techniques) are limited to a certain spectral range in which the cavity mirrors exhibit maximum reflectivity. Generally, the higher the mirror reflectivity, the narrower is the range of its high reflectivity performance and therefore the narrower the spectral region of the setup's maximum sensitivity. This restricts the spectral coverage of cavity-enhanced absorption spectra taken with one set of mirrors. On the one hand, a wide spectral range is needed to detect multiple trace constituents under the same experimental conditions. On the other hand, truly broad spectral ranges can only be achieved by using mirrors with modest reflectivity. The corresponding decrease of sensitivity can only be compensated by increasing the length of the cavity. For example, in first approximation the sensitivity of an absorption cavity of length l formed by mirrors with $R = 0.999$ is the same as that of a cavity formed by mirrors with $R = 0.99$ and a length of $10\,l$. Hence long optical cavities are obviously suited for highly sensitive true broadband absorption measurements provided the spectral reflectivity range of the mirrors can be fully covered by the light source employed.

Third, for absolute concentrations to be retrievable with IBBCEAS, the mirror reflectivity must be known. Independent reflectivity calibration measurements are therefore essential. In the case of enclosed cavities, mirror reflectivities can be measured using a known amount of a calibration gas [33–36], but this approach is often impractical for open-path configurations. A straightforward way of establishing the mirror reflectivity with acceptable uncertainty using an antireflection-coated optic of known loss will be outlined.

In this publication we demonstrate that very long optically stable cavities (~20 m length) can be constructed in open-path configuration for monitoring atmospheric trace constituents and aerosol extinction. The main target species were NO_3 and NO_2. The optical design of the IBBCEAS instrument, its mechanical stability, and issues concerning the cavity alignment will be addressed. The data presented were taken during an intercomparison campaign of instruments for the detection of NO_3 and N_2O_5, which took place at the SAPHIR atmospheric simulation chamber at the Forschungszentrum Jülich in June 2007 [39]. The SAPHIR chamber is an ideal facility to test and characterize the performance of our IBBCEA apparatus for specific atmospheric scenarios and to develop appropriate analysis procedures for the cavity-enhanced broadband absorption spectra. SAPHIR is equipped with a set of detection instruments that provide accurate concentrations of water and NO_x (among other species) as well as the chamber temperature as a function of time. Following on from the SAPHIR simulation experiments, the instrument's performance in a field trial

at Roches Point in County Cork, Ireland, will also be briefly outlined.

2. Experiment

In IBBCEAS, light from an incoherent broadband light source is coupled into an optically stable cavity formed by two mirrors of high reflectivity (R). The transmission spectrum of the cavity is measured first in a clean atmosphere (I_0) and then in the sample atmosphere (I) over a certain path length (L), which is not necessarily equal to the separation of the cavity mirrors (l). The extinction of the gas mixture (ε) as a function of wavelength (λ) is given by [32,37]

$$\varepsilon(\lambda) = \sum_i \sigma_i(\lambda) \int_0^L n_i(x)\mathrm{d}x = \frac{1}{L}\left(\frac{I_0}{I} - 1\right)(1 - R), \quad (1)$$

where $\sigma_i\,(\mathrm{cm^2\,molecule^{-1}})$ is the wavelength-dependent absorption cross section of species i and $n_i\,(\mathrm{molecule\,cm^{-3}})$ its number density.

A. Instrument Setup

The instrument described here was designed to quantify NO_3 concentrations based on its strong $B \leftarrow X$ absorption band with a maximum at 662 nm; however, the setup is readily adapted to other wavelength regions in the visible and near-UV. The instrument consisted of a transmitter unit and a receiver unit, each housing one of the cavity mirrors. The two units could be separated by any arbitrary distance in an open-path configuration depending on the mirrors' radii of curvature. Schematics of the optical components of the transmitter and receiver units of the instrument are shown in Fig. 1.

The transmitter unit housed a short-arc Xe lamp running in a so-called hot spot mode. In this mode a small plasma spot (~150 μm) with a spectral radiance of 18 $\mathrm{W\,cm^{-2}\,sr^{-1}\,nm^{-1}}$ at 400 nm is formed close to the cathode surface [40]. The small spot size gave this lamp unique imaging properties compared to the generally diffuse arcs of conventional Xe lamps. The light from the lamp was imaged onto an iris using two off-axis parabolic mirrors as shown in Fig. 1(a). Between the parabolic mirrors the wavelength range was selected with an interference filter (Andover 650FS80-50) between ~610 and 720 nm. A fraction of the light was focused onto a quadrant detector while with the main beam an image of the hot spot was formed in the plane of an iris. Although the hot spot provides nearly 20 times the brightness compared to diffuse arcs, the spot tended to wander around the cathode. This arc wandering was compensated by stabilizing the image of the hot spot with a feedback loop between the quadrant detector and a piezo-mounted plane mirror placed between the lamp and the first parabolic mirror [see Fig. 1(a)]. A telescope imaged the iris aperture at the center of the open-path cavity. For the measurements at the Forschungszentrum Jülich, the transmitter unit was placed at one end of the SAPHIR chamber and the receiver unit was placed at the other end, giving a

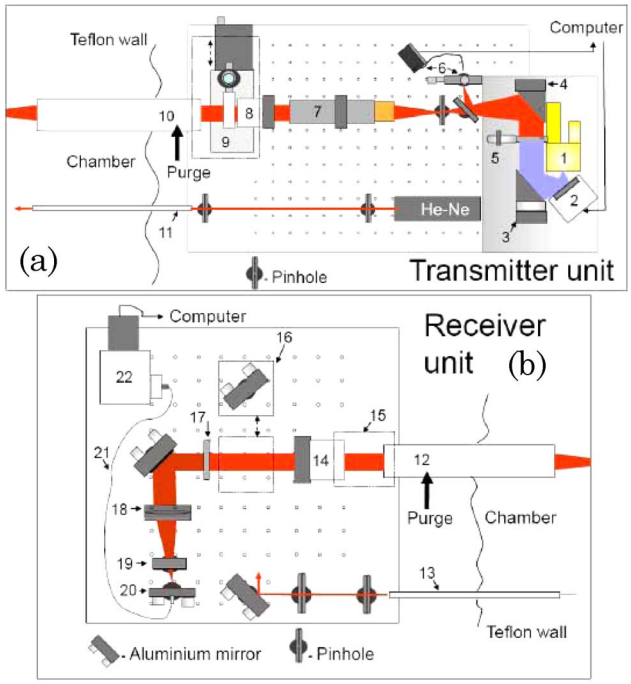

Fig. 1. (Color online) (a) Transmitter unit: 1, short-arc Xe lamp; 2, piezo-mounted plane mirror; 3,4, off-axis parabolic mirrors; 5, interference filter; 6, quadrant detector and control electronics; 7, telescope; 8, highly reflective cavity mirror; 9, low-loss optic assembly on translation stage; 10,11, stainless steel pipes for broadband beam and He–Ne laser beam, respectively. (b) Receiver unit; 12,13, stainless steel pipes for broadband beam and He–Ne laser beam, respectively; 14, highly reflective cavity mirror; 15, Teflon film joint; 16, movable mirror to couple in He–Ne laser beam; 17, color filter (RG630); 18, focusing lens; 19, short-pass filter (cutoff ~700 nm); 20, fiber bundle holder; 21, fiber bundle; 22, monochromator and CCD detector.

mirror separation of $l = (20.13 \pm 0.05)$ m. The cavity was formed by dielectric mirrors (Layertec GmbH) with a diameter of 4 cm, a radius of curvature of 21 m, and a nominal reflectivity of about 0.999 at 660 nm [compare Fig. 2(c)].

The receiver unit housed the second cavity mirror. Light transmitted by the cavity was further filtered with a long-pass cutoff filter (RG630 colored glass) and a 700 nm short-pass interference filter (Thorlabs FES0700) to ensure that light outside the mirror reflectivity range is eliminated. The light was focused into a fiber bundle (1 mm diameter) and connected to the 100 μm entrance slit of a monochromator (holographic grating, 1200 lines/mm) that had a CCD detector (Andor DV401, pixel size 26 μm) attached to it. The spectral resolution of the detection system was approximately 0.6 nm. The spectrometer wavelength scale, which was calibrated daily using both a Ne pen lamp and a He–Ne laser, was accurate to better than 0.01 nm. The He–Ne laser was housed in the transmitter unit and served as an important tool for aligning the cavity (see below). An acquisition time of 5 s was used for all the measurements.

The transmitter and receiver units were each equipped with a 1 m stainless steel pipe (57 mm

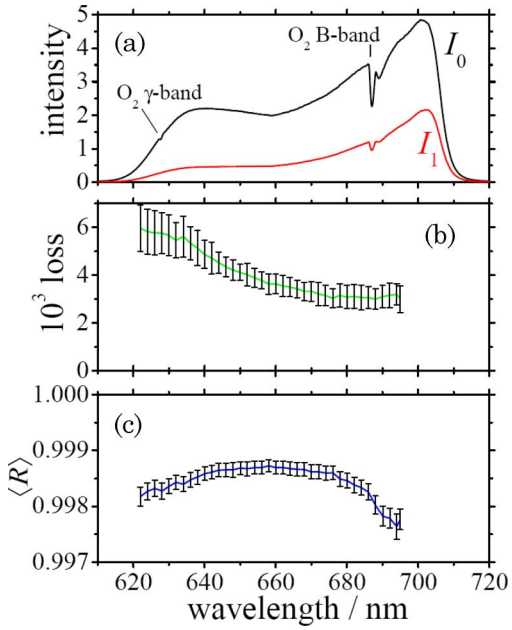

Fig. 2. (Color online) (a) Typical transmission spectra of the cavity (in units of 10^6 counts) containing clean air only (I_0), and with a low loss substrate in the cavity (I_1). The spectra represent the average of 100 spectra, each having a 5 s acquisition time. The γ- and B-band of O_2 at around 624 nm and 687 nm, respectively, are the only absorption features in this spectrum. (b) Loss spectrum $L(\lambda)$ of the antireflection-coated substrate measured with pulsed cavity ring-down spectroscopy in a 2 m cavity. The error bars correspond to the 1σ standard deviation of seven measurements of loss $L(\lambda)$. (c) Average mirror reflectivity, $\langle R \rangle$, of 11 individual reflectivity measurements taken on each day of the campaign. The error bars represent the corresponding 1σ standard deviation.

diameter) pointing from the cavity mirrors along the optical axis of the cavity. Each pipe was mounted to the unit's chassis to support its weight. A seal was made between the pipes and the adjustable mirror mounts of the cavity mirrors using flexible Teflon foil in each unit. The pipes served three purposes: First, they allowed the mirrors to be purged with an inert gas to keep the mirrors clean. The purge gas in the present case was N_2 at a flow rate of $\sim 10\,\mathrm{dm^3\,min^{-1}}$. Purging the mirrors reduced the effective cavity length to $L = (18.27 \pm 0.20)\,\mathrm{m}$. Second, on the receiver side of the setup the pipe reduced stray light entering the detection system. Third, for the intercomparison campaign the pipes were necessary to attach the instrument to the SAPHIR chamber and to make a seal with its Teflon wall. Apart from the pipes for the broadband light beam, two smaller pipes (25 mm diameter) were also used to form openings for the He–Ne laser beam. The small pipes were sealed on one side with a simple optical window.

B. Cavity Alignment

The cavity was aligned using a He–Ne laser beam passing through two pinholes in each of the units to define a secondary axis parallel to the cavity axis. For coarse alignment, the cavity mirror on the receiver side was removed. The He–Ne laser beam was sent along the secondary axis from the transmitter unit to the receiver unit, where it was directed onto the cavity axis and returned to the high reflectivity mirror in the transmitter unit. The cavity mirror in the transmitter unit was adjusted to reflect the laser beam back onto itself. All optics inside the chassis of the receiver unit rested on a home-made x, y, z translation stage, which could also be rotated about the azimuthal and polar angles. This enabled all relevant degrees of freedom to be adjusted in order to align the receiver unit with respect to the transmitter unit. The second cavity mirror was then put into place and the He–Ne laser beam was reflected back onto itself again. By removing the interference filter in the transmitter unit, spectrally broad light from the arc lamp was let into the cavity and the telescope was adjusted to focus the image of the hot spot in the center of the SAPHIR chamber. The optical filters were then put into place and the cavity mirrors were fine tuned to optimize the intensity of the cavity transmission once an initial transmission was observed. At optimum alignment it was even necessary to attenuate the light to avoid saturating the CCD detector (which indicates that even higher reflectivity mirrors could be used with this setup to further improve the sensitivity). The transmitter and receiver units were mounted to a rigid frame on top of a permanently installed UV multipass DOAS system, which itself rested on a very heavy concrete block that was largely decoupled from the SAPHIR chamber. The mechanical stability of the setup was excellent. It ran without any substantial realignment of the cavity for the 12 days of the campaign. Very good stability was again observed using an 8.6 m cavity in a field trial at Roches Point (Ireland), during which the mechanical properties of the instrument were satisfactory despite exposure to persistent high winds.

C. Calibration of Mirror Reflectivity

An important experimental aspect of the open-path IBBCEA approach is the calibration of the cavity mirror reflectivity, which is necessary to retrieve absolute number densities of absorbing species; see Eq. (1). In the case of an enclosed cavity, the mirror reflectivity $R(\lambda)$ can be determined from transmission spectra with and without a known concentration of a calibration gas in the cavity, whose absorption cross section is known as a function of wavelength [31,33,34]. With a long open-path setup this approach is not practical. However, by using an antireflection-coated optical substrate of known loss, $L(\lambda)$, instead of a calibration gas, the mirror reflectivity can be determined by

$$R(\lambda) = 1 - \left[\frac{I_1(\lambda)}{I_0(\lambda) - I_1(\lambda)} L(\lambda)\right], \qquad (2)$$

where $I_1(\lambda)$ and $I_0(\lambda)$ are the respective transmission spectra of the cavity with and without the low-loss substrate [typical examples are shown in Fig. 2(a)].

The loss

$$L(\lambda) = \frac{d}{c}\left(\frac{1}{\tau_2(\lambda)} - \frac{1}{\tau_1(\lambda)}\right) \quad (3)$$

was measured after the campaign in the laboratory by CRD spectroscopy over the range from 630 to 690 nm using a tunable dye laser [ideally the low-loss calibration measurements should have been taken before and after employment of the instrument at the SAPHIR chamber; however, the CRD system only became available immediately after the campaign so that it was not possible to measure $L(\lambda)$ in advance of the intercomparison]. In Eq. (3), $\tau_1(\lambda)$ and $\tau_2(\lambda)$ are the ringdown times measured without and with the substrate in a cavity of length $d = 2$ m, respectively, and c is the speed of light in air. The measured loss as a function of wavelength is shown in Fig. 2(b). The error bars in the figure are based on the reproducibility of seven loss measurements, where the cavity was realigned from scratch each time.

In the open-path instrument the low-loss optic [$L(\lambda) < 0.001$, Layertec] was placed on a translation stage that was sealed in a Teflon foil assembly between one of the cavity mirrors and the steel pipe [see Fig. 1(a)]. Reflectivity calibration measurements were performed daily during the campaign. The average of these reflectivity measurements, $\langle R \rangle$, is shown in Fig. 2(c).

There are uncertainties associated with the outlined calibration of R, some of which are difficult to quantify: First, the CRD loss measurement of $L(\lambda)$ was performed with a short cavity. Even though the measured loss should in first approximation be independent of the cavity length, possible systematic errors cannot be easily estimated without CRD measurements using a long cavity. Second, the loss of the calibration optic is measured for a beam traveling along the optical axis of the cavity. The broadband application however uses the full diameter of the cavity mirrors and integrates over all off-axis modes of the resonator. The inherently different average residence time of photons propagating off-axis in the cavity causes R in Eq. (1) to represent an effective (empirical) reflectivity [37], which is generally slightly smaller for broadband applications than for on-axis CRD. The on-axis loss calibration of the substrate and its subsequent application in a cavity where its full area is utilized leads to systematic errors that are again difficult to quantify without additional information on mode-dependent loss mechanisms in the cavity [37]. The discrepancy between the true broadband effective R and the reflectivity found by the calibration procedure outlined here is expected to be small (a few percent).

Furthermore, the retrieved reflectivity was not critically dependent on the orientation of the low-loss substrate with respect to the cavity axis. Deliberately misaligning the substrate by up to $\pm 2.5°$ between the substrate's normal and the cavity axis resulted in errors that are small in comparison to the uncertainty of $L(\lambda)$. The accuracy with which R can be determined is therefore not compromised by small misalignments. This insensitivity with respect to misalignment is due to the broadband antireflection coating of the substrate.

D. Instrumentation at SAPHIR

Long path DOAS: NO_3 was measured by DOAS with a multiple reflection setup [41,42]. Light from a conventional Xe arc lamp (Osram, XBO 75 W/2) was directed into a multireflection cell of 20 m base length, which was set up along the axis of the cylindrical SAPHIR chamber. After 48 passes equaling an optical path length of 960 m the light was dispersed by a Czerny–Turner spectrograph with a blazed holographic grating (Jobin-Yvon, HR 460). Absorption spectra were recorded with a resolution of 0.4 nm in the range between 603 and 691 nm using a photodiode array (Hamamatsu, S3904, 1024 pixels). The detector array was connected to a computer via a controller (Hoffmann Messtechnik). NO_3 mixing ratios, determined using the DOAS analysis procedure (DOASIS [43]), are based on reference data by Yokelson *et al.* [44], Voigt *et al.* [45], and Rothman *et al.* [46]. The precision of the DOAS NO_3 detection was appoximately 10 pptv. An additional uncertainty of maximum 20 pptv was caused by a drift in the optical setup. The time resolution of the DOAS instrument depended on the light throughput and was between 65 and 95 s.

Chemiluminescence analyzer: NO, NO_2, and O_3 mixing ratios were measured with a chemiluminescence analyzer (Eco Physics, CLD 780TR) [47]. NO was detected after reaction with an excess of O_3, and the sum of NO and NO_2 is detected after photolytic conversion of NO_2 to NO (Eco Physics PLC760). O_3 was detected after reaction with excess NO. The analyzer's detection limits were 5 and 10 pptv with accuracies of 5% and 10% for NO and NO_2, respectively, for an acquisition time of 90 s.

Hygrometer: The chamber's water vapor content was measured with a dew point hygrometer (General Eastern, Hygro M4) with a detection limit of 20 ppmv (dew point −60 °C) for a sampling time of 10 s.

3. Analysis of Spectra

Spectral windows of 10–15 nm were used to quantify the absorption of particular molecules. These wavelength ranges were selected to include appropriate absorption features of the target molecule while avoiding significant absorption structures from other species. The NO_3 absorption was analyzed between 658 and 668 nm, and the NO_3 concentrations were quantified using absorption cross sections by Yokelson *et al.* [44]. The cross sections from Ref. [44], valid for 298 K, were scaled to the chamber temperature using the temperature dependence of the NO_3 absorption reported by Orphal *et al.* [48]. The analysis of NO_2 was carried out in the 630–645 nm window to minimize water vapor interference. Reference NO_2 absorption cross sections from Burrows *et al.* [49]

were used. All reference spectra were convoluted with the instrument function of approximately 0.6 nm. For spectral fitting, the extinction coefficient, $\varepsilon(\lambda)$, is described by

$$\varepsilon(\lambda) = a_0 + a_1\lambda + a_2\lambda^2 + a_3\sigma_{H_2O}(\lambda) + a_4\sigma_{NO_3}(\lambda) + a_5\sigma_{NO_2}(\lambda), \quad (4)$$

where σ_i is the reference absorption cross section (cm^2 $molecule^{-1}$) of species i, and the coefficients a_3 to a_5 are the number densities of these species. The second-order polynomial term in Eq. (4) accounts for the baseline offset of the extinction spectrum, which could arise from scattering from aerosols, fluctuations in the lamp intensity, and other unspecified loss processes. The linear component, $a_1\lambda$, of the polynomial function largely accounts for the absorption of O_3, whose broad, unstructured absorption band (Chappuis band) covers the spectral region of interest. Explicitly including the O_3 absorption with the additional term $a_6\sigma_{O_3}$ did not significantly improve the fit to the measured extinction, nor did the values of a_6 represent meaningful O_3 number densities. O_3 concentrations thus cannot be easily determined with the analysis procedure outlined here. A MATLAB routine for singular value decomposition (SVD) based on a linear least-squares procedure [50] was used to fit Eq. (4) to the measured extinction coefficient. The results from the SVD approach did not differ appreciably from those obtained with a nonlinear Levenberg–Marquardt routine. Although SVD analysis depends on the size of the fit range, there is no start parameter selection that may influence the fit results, and the inherent degree of correlation of parameters in Eq. (4) is not affected by this analytical approach. Moreover, the SVD analysis was much faster than iterative methods, an important practical consideration for the large data sets generated. The analysis procedure also allowed for a small shift, $\Delta\lambda$, in the wavelength of the reference spectra ($\lambda' = \lambda + \Delta\lambda$). For each day a fitted spectrum $\varepsilon(\lambda)$ containing NO_3 absorption was gradually shifted over a wavelength range of ± 0.3 nm in steps of 0.001 nm. $\Delta\lambda$ was determined by the shift that yielded the minimum least-squares sum between the fitted and the measured spectrum. The shifts were always smaller than the spectral resolution of the spectrometer ($\sim$0.6 nm), and the average day-to-day shift over the campaign was $\Delta\lambda = (-0.27 \pm 0.02)$ nm (1σ error). For the data used in this paper (15 June 2007) $\Delta\lambda$ fluctuated around -0.26 nm before and around -0.23 nm after the introduction of water vapor to the chamber. It was found that by using one wavelength shift for the entire day, the consequence for the retrieved trace gas concentrations was small. The NO_3 mixing ratios did not change by more than (0.08 ± 0.26) pptv when $\Delta\lambda$ was varied for each measurement compared to when the shift was fixed at the same value of $\Delta\lambda = -0.26$ nm for the entire day (on 15 June). This uncertainty of the mixing ratios is smaller than the estimated precision of the measurements (see below) and hence justifies the use of only one shift value, $\Delta\lambda$, per day.

Standard uncertainty propagation was used to estimate the uncertainty of the retrieved number densities. The uncertainty in the measured sample extinction, $\Delta\varepsilon$, from Eq. (1) is given by

$$\Delta\varepsilon^2 = \left|\frac{dn_i}{d(1-R)}\right|^2 \Delta(1-R)^2 + \left|\frac{dn_i}{dL}\right|^2 \Delta L_{eff}^2 + \left|\frac{dn_i}{dI_0}\right|^2 \Delta I_0^2, \quad (5)$$

where the fractional uncertainties of the parameters are estimated to be 8% for $(1-R)$, 1% for the effective cavity length L, and 5% for I_0. The uncertainty in the measured extinction is therefore ~10%. Furthermore, spectral analysis using Eq. (4) contributes additional uncertainties to the retrieved concentrations of absorbing species. These uncertainties arise through the dependence of the fit on the spectral window (3%) and the uncertainties of the reference absorption cross sections, which are ~10% for the NO_3 absorption cross section [44] and ~3% for the NO_2 absorption cross section [49]. Assuming that the uncertainty of reference spectra lies in their magnitude across the spectral window, contributions from species apart from the species of interest can be ignored in the fit since the fitting parameter yielding the associated number density of the species should scale accordingly. Cross sensitivities in the fit between different species only become important close to the detection limit of the target species, where the precision dominates the uncertainty of the number density retrieval. The overall uncertainty in the retrieved number density of species i, $n_{i,fit}$, is then

$$\Delta n_{i,fit}^2 = \Delta(\text{range})^2 + \left|\frac{dn_i}{d\varepsilon}\right|^2 \Delta\varepsilon^2 + \left|\frac{dn_i}{d\sigma_i}\right|^2 \Delta\sigma_i^2. \quad (6)$$

The overall uncertainty in NO_3 concentrations is 18%, while NO_2 concentrations have a 14% uncertainty.

Fluctuations in the light intensity degraded the precision of the retrieved concentrations on the timescale of the measurements. Independently monitoring the lamp output as a basis for normalizing cavity spectra should improve measurement precision but was not implemented during the intercomparison campaign. In the absence of direct lamp intensity measurements, the effect of fluctuations in lamp intensity was substantially reduced by normalizing cavity spectra based on the intensity transmitted through the cavity at 684 nm, a region with very small molecular absorption. The time series of the intensity measurements at 684 nm was smoothed by fitting a cubic spline to the data points [Fig. 5(d)]. The ratio of the measured intensity at 684 nm for each individual spectrum to that of the

smoothed value was then used to scale the overall intensity spectrum, I, before the extinction coefficient was calculated using Eq. (1). This procedure effectively discarded short-term lamp intensity fluctuations. Longer term drifts in the transmitted intensity (following introduction of aerosols, for instance) did not erroneously scale the spectra and the corresponding retrieved concentrations. In the instrument that was later deployed in the field, modifications were made to record the lamp intensity directly from the quadrant detector in order to normalize the intensity spectra.

4. Results and Discussion

A. Detection of NO_3 and NO_2 in the SAPHIR chamber

The NO_3 and NO_2 data presented below are from the chamber experiment on 15 June 2007, in which atmospherically realistic concentrations of these species were present in the chamber together with water vapor and $(NH_4)_2SO_4$ aerosol. O_3 concentrations were maintained between 100 and 200 ppbv except when the chamber was being purged. This experiment thus serves as a suitable proxy for the real atmosphere where multiple extinction processes occur. While a discussion of the results of the NO_3 and NO_2 intercomparison is beyond the scope of this paper, the IBBCEAS system showed good overall agreement with other techniques for both species [39,51,52]. The approaches to NO_3 detection applied during the campaign comprised extractive techniques [pulsed CRD spectroscopy (off-axis and also in combination with CEAS) and broadband CRD spectroscopy] and open-path methods (DOAS and broadband CEAS). The most sensitive instruments achieved a detection limit for NO_3 of a few pptv in a few seconds or better [7,9,53]. As opposed to extractive methods, where one of the main challenges lies in the calibration of inlet losses, the prime difficulty in broadband open-path methods is the retrieval of concentrations from extinction spectra that are based on a variety of loss processes.

For NO_3 and NO_2 the retrieval of concentrations is complicated by a water absorption band that overlaps the strong NO_3 $B \leftarrow X$ absorption band with a maximum at 662.7 nm and, to a lesser extent, the 630 nm to 645 nm window used to quantify NO_2 concentrations. Apparent deviations from the Beer–Lambert law arise because the water lines are much narrower than the resolution of the monochromator. The problem caused by not fully resolving the absorption structure of water vapor was already reported by Bitter *et al.* [14], who observed multiexponential ringdown decays with the BBCRD spectroscopy technique and outlined a procedure to account for it. In the following, we describe an approach to treat this effect in IBBCEA spectra.

To properly describe the absorption of water vapor, a concentration-corrected absorption cross section, σ'_{H_2O}, was calculated for each spectrum measured, i.e., for each water concentration that occurred in the chamber. Starting with an arbitrary synthetic spectrum, $I_0(\lambda)$, with a data point increment of 0.001 nm, Eq. (1) was used to calculate a high-resolution cavity transmission spectrum, $I(\lambda)$, using the water absorption data from the HITRAN database [46], the water vapor concentration in the chamber, and the calibrated mirror reflectivity spectrum. $I(\lambda)$ was then convoluted with the 0.6 nm resolution of the monochromator, and Eq. (1) was applied a second time to retrieve the concentration-corrected absorption cross section, σ'_{H_2O}, for water vapor at that concentration. A different σ'_{H_2O} was calculated for each spectrum and the entire process was automated. The effect of non-Beer–Lambert behavior on the water vapor absorption cross section is illustrated in Fig. 3, together with the results obtained by directly convoluting the HITRAN water cross sections (corresponding to the low concentration limit). As expected, apparent deviations from Beer–Lambert behavior are greatest for large absorption features. In principle, the same procedure should be applied to the structured NO_2 absorption cross sections, but the small absorption of NO_2 in this region made this unnecessary in practice.

The correction procedure outlined above depends on an independent measurement of the water vapor concentration. In principle it should also be possible to retrieve the water vapor concentrations directly from the spectra using, for example, a lookup table correlating water concentrations with the magnitude of prominent absorption features. This procedure would provide the water vapor concentration as a routine result and eliminate the need for monitoring the water vapor concentrations separately. However, establishing an adequate lookup table in practice is a nontrivial and formidable task, as one has to account for the concentration dependence of the water absorption for a given IBBCEA setup (using a specific $R(\lambda)$ and effective cavity length L) and the effect of other extinction processes.

Cavity transmission spectra taken at 4:09 and at 9:58 a.m. are shown in Fig. 4(a) between 610 and

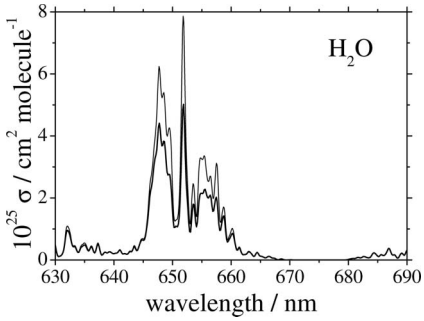

Fig. 3. (Color online) Black: absorption spectrum of water vapor calculated by convoluting HITRAN cross sections [46] with the spectrometer's resolution of 0.6 nm. Thick lower trace: spectrum of the concentration-corrected H_2O cross sections calculated with Eq. (1) as outlined in the text using a number density of water of 2.72×10^{17} molecules cm^{-3}, an 18.27 m cavity length, a 0.6 nm spectrometer resolution, and the reflectivity spectrum measured on 15 June 2007.

720 nm. At the early time (thin curve) the chamber contained only clean dry synthetic air; at the later time (thick curve) it was filled with water vapor and high concentrations of nitrogen oxides. The extinction spectrum for the NO_3 window derived from the intensity measurements in Fig. 4(a) is shown in Fig. 4(b). The number density of water was 4×10^{17} molecules cm^{-3} (60% relative humidity). Equation (4) was fitted to the extinction data using the concentration-corrected [solid curve in Fig. 4(b)] and the uncorrected (dashed curve) water cross sections. The quality of the fit to the measured spectrum improves markedly when using the corrected water absorption cross section: the 1σ rms value of the fit residual obtained using the corrected water absorption cross section is about 0.55×10^{-9} cm^{-1}, compared to 2.03×10^{-9} cm^{-1} from the uncorrected water cross section. Properly accounting for the water absorption is particularly important at low NO_3 concentrations because typical atmospheric concentrations of water vapor mask the NO_3 absorption. After subtracting the fitted water absorption from the measured spectrum, the NO_3 absorption peak is readily distinguished from the background extinction [Fig. 4(c)]. The NO_3 concentration obtained in this example

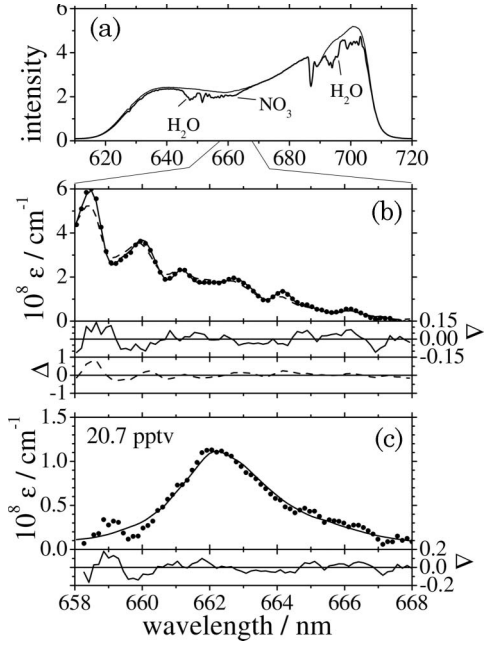

Fig. 4. (Color online) (a) Typical cavity transmission spectra (in units of 10^6 counts) in the absence (thin upper trace) and presence of water vapor and NO_3 (lower trace). Measurement taken with 5 s acquisition time at 9:58 a.m. on 15 June 2007. (b) Corresponding measured extinction (solid circles) in the region between 658 nm and 668 nm. The solid and dashed curves represent SVD fits of Eq. (4) to the experimental spectrum with and without using concentration-corrected H_2O cross sections, respectively (see Fig. 3). (b) and (c) show the corresponding fit residuals Δ (axis units given in 10^{-8} cm^{-1}). (c) Extinction (filled circles) from (b) after removing the water vapor absorption; the contribution of NO_3 absorption to the fit is shown as a solid curve. The mixing ratio of NO_3 was determined to be approximately 20.7 pptv. The lower panel shows the corresponding fit residuals, Δ in units of 10^{-8} cm^{-1}.

was (20.7 ± 1.0) pptv, and the NO_2 concentration was (5 ± 1) ppbv.

The time dependence of the NO_3 and NO_2 concentrations during the chamber experiment on 15 June 2007 is shown in Figs. 5(a) and 5(b). The chamber atmosphere was initially dry (−58 °C dew point) and free of aerosol. NO_3 was formed at moderately high concentrations by adding 1.5 ppbv of NO_2 in the presence of approximately 180 ppbv of O_3 (see the Fig. 5 caption). The precision of temporally close measurements was around 1.3 pptv when the NO_3 concentration was around 100 pptv, while the NO_2 precision was about 2 ppbv when the concentration was 5 ppbv. The precision of the NO_2 detection is worse than that of typical chemiluminescent NO_x detectors, but the 5 s sampling time is also an order of magnitude smaller than that of the chemiluminescent analyzer attached to the SAPHIR chamber, which had a sampling time of about 1 min. The chamber was purged with humid synthetic air between 8:55 and 9:52 a.m., resulting in a sharp decrease in NO_3 and NO_2 concentrations and rapid

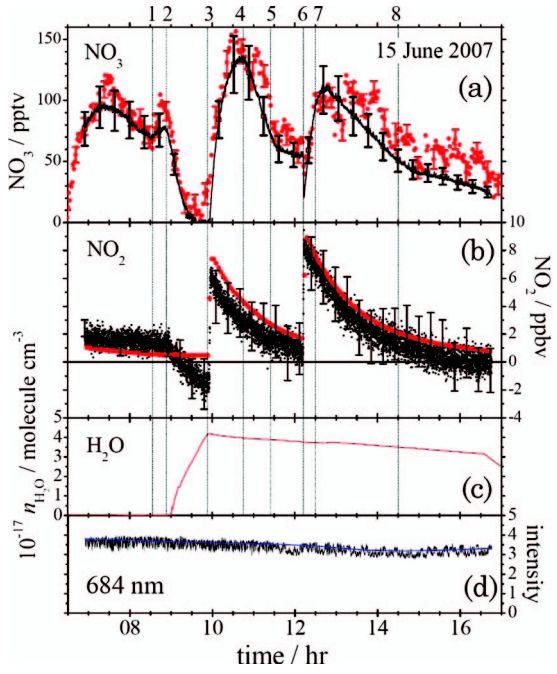

Fig. 5. (a) Time series of NO_3 mixing ratios measured by IBBCEAS (black data) and long path DOAS (red data). (b) Time series of NO_2 mixing ratios measured by IBBCEAS (black data) and the chemiluminescence analyzer (red data). (c) Time series of H_2O number densities measured with a dew point hygrometer. (d) Cavity transmission (in units of 10^6 counts) at 685 nm (black) and cubic spline through data (blue). The SAPHIR chamber event sequence on 15 June 2007 was: 6:11–fan on, 6:15–180 ppbv of O_3 added, 06:22–1.5 ppbv of NO_2 added, 8:33–fan off (1), 8:52–fan on (2), 8:55–flushing of chamber with clean humid air started (2), 9:52–flushing of chamber ended (3), 9:53–80 ppbv of O_3 added (3), 9:53–2 ppb of NO_2 added (3), 9:56–9 ppbv of NO_2 added (3), 10:45–addition of $(NH_4)_2SO_4$ aerosol started (4), 11:25–addition of aerosol ended ($5\,\mu g\,m^{-3}$) (5), 12:12–9 ppbv of NO_2 added (6), 12:30–addition of $(NH_4)_2SO_4$ aerosol started (7), 14:30– addition of aerosol ended ($12\,\mu g\,m^{-3}$) (8).

humidification of the chamber atmosphere to 60% relative humidity [Fig. 5(c)]. NO_3 is essentially absent from the chamber between 9:30 and 9:52 a.m., when an average concentration of 0.4 pptv was found with a precision of 0.9 pptv. During the same time slightly negative NO_2 concentrations were retrieved. Although the negative NO_2 values were close to the experimental uncertainty, the retrieval of NO_2 concentrations appeared to be slightly dependent on the H_2O or the O_3 absorption within the fitting range. Further loading of O_3 and the addition of 9 ppbv NO_2 at 9:56 a.m. rapidly regenerated NO_3.

$(NH_4)_2SO_4$ aerosol was introduced into the chamber between 10:45 and 11:25 a.m. to a loading of $5\,\mu g\,m^{-3}$. A constant rate of decrease of NO_3 was observed over this interval and arises from the hydrolysis on particles of N_2O_5, with which NO_3 is in equilibrium [11]. The rate of NO_2 loss in the humid atmosphere appeared to be independent of the particle loading according to the data presented in Fig. 5(b).

A further 9 ppbv NO_2 was injected into the chamber at 12:12 p.m. The NO_3 concentration responded with a sharp initial decrease (by shifting the equilibrium $NO_2 + NO_3 \leftrightarrow N_2O_5$ to favor N_2O_5 formation). This decrease was followed by a rapid increase in the NO_3 concentration to over 100 pptv as NO_2 reacted with excess O_3 to produce more NO_3. A second loading of aerosol to $12\,\mu g\,m^{-3}$ was added between 12:30 and 14:30 p.m. NO_3 concentrations again decreased over this period. The slower decay of NO_3 in this case is attributed to the higher concentration of N_2O_5 acting as a reservoir for NO_3.

The retrieved NO_3 concentrations from the IBBCEAS system can also be compared with the data from the established DOAS technique [Fig. 5(a)]. The agreement over the 10 h of the experiment is quite satisfactory both at high concentrations and at low concentrations; neither aerosols nor water vapor affect the NO_3 concentrations retrieved with either technique. The results are highly correlated [39] and differ mainly in the acquisition time (5 s for IBBCEAS versus 90 s for DOAS) and in the precision of the measurements. Reasonable agreement in the measured NO_2 concentrations is also achieved between IBBCEAS and the chemiluminescent detector [Fig. 5(b)]. Both instruments yield similar NO_2 concentrations following the introduction of NO_2 at 9:56 a.m. and 12:12 p.m. A small discrepancy of about 1 ppbv is apparent at the start of the experiment and with the flushing of the chamber. Careful selection of the NO_2 retrieval window in the IBBCEAS experiments may reduce or eliminate the cross sensitivity to water vapor (or O_3) absorption.

Generally, the noise on the IBBCEAS data is considerably smaller than that on the LP-DOAS measurements due to the better sensitivity of the IBBCEAS instrument. The difference is usually within the combined uncertainty of both methods. It should be noted, however, that after 1 p.m. on 15 June, a monotonic decrease in the NO_3 concentration was expected as observed by the IBBCEAS instrument. The apparent rapid fluctuations in NO_3 concentrations found with the long path DOAS setup [Fig. 5(a)] are due to the precision of the instrument and do not represent an increased uncertainty in the IBBCEAS setup. The choice of the fitting range and a discussion of various different experimental aspects of the two methods are beyond the scope of this study.

B. Aerosol Extinction

As indicated by the polynomial $(a_0 + a_1\lambda + a_2\lambda^2)$ in Eq. (4), it is necessary to account for the sample's background losses and their temporal changes. Background losses can be assigned to aerosol extinction as long as other contributions from molecular absorbers and instrumental artifacts have been accounted for. Aerosol extinction based on Eq. (4) is very sensitive to the value of I_0. While the normalization procedure described above accounts for rapid fluctuations in the intensity, and hence in I_0, long-term changes in the lamp intensity are difficult to distinguish from aerosol extinction in the chamber. An alternative approach to retrieving the aerosol extinction is based on using the change in the fractional absorption of a known absorption feature. The fractional absorption changes because aerosol and other extinction processes shorten the effective path length, which is defined as $L_{\text{eff}} \equiv L/(1-R)$. This effect is illustrated in Fig. 2(a), where the O_2 absorption at 687 nm is proportionally smaller in I_1 (measured with an extra loss per pass in the cavity) than in I_0. O_2 is particularly appropriate for this purpose because its concentration is constant, and thus the absorption coefficient in the maximum of the B-band at around 687.3 nm is also constant in the real atmosphere. Furthermore, the B-band falls within the spectral region where other molecular absorptions are small and where it was readily observable with our spectrometer [see Fig. 4(a)].

For an atmospheric sample whose total extinction, $\varepsilon_T = \varepsilon_B + \alpha$, is the sum of a contribution from background extinction, ε_B, and sample absorption, α, we can define three intensities transmitted through the cavity associated with these extinctions. These are (i) I_0, the intensity in the absence of any extinction ($\varepsilon_T = 0$); (ii) I_B, the intensity when *only* spectrally broad and unstructured background extinction is present ($\varepsilon_T = \varepsilon_B$), such that from Eq. (1)

$$\varepsilon_B = \left(\frac{I_0 - I_B}{I_B}\right)\left(\frac{1-R}{L}\right) = \left(\frac{\Delta I_B}{I_B}\right)\left(\frac{1-R}{L}\right), \qquad (7)$$

where $\Delta I_B \equiv I_0 - I_B$; and (iii) I, the intensity in the general case in which there is both a background extinction as well as some (structured) sample absorption

$$\varepsilon_T = \varepsilon_B + \alpha = \left(\frac{I_0 - I}{I}\right)\left(\frac{1-R}{L}\right) = \left(\frac{\Delta I_B + \Delta I_A}{I}\right)\left(\frac{1-R}{L}\right), \quad (8)$$

with $\Delta I_A \equiv I_B - I$ arising from structured absorption and ΔI_B attributed to the background extinction. It is clear that $I < I_B < I_0$ and that only one intensity can be measured at any given time. Substituting Eq. (7) into Eq. (8) and solving for α gives

$$\alpha = \left(\frac{\Delta I_A}{I}\right)\left(\frac{1-R}{L}\right)\left(1 + \frac{\varepsilon_B L}{1-R}\right) = \left(\frac{\Delta I_A}{I}\right)\left(\frac{1}{L_{\text{eff}}}\right)(1 + \varepsilon_B L_{\text{eff}}). \quad (9)$$

Equation (9) shows in comparison with Eq. (1) that the effective path length, $L_{\text{eff}} = L/(1-R)$, is shortened in the presence of additional extinction processes to $L'_{\text{eff}} = L_{\text{eff}}/(1 + \varepsilon_B L_{\text{eff}})$. Equation (9) can be rewritten as

$$\varepsilon_B = \alpha\left(\frac{I}{\Delta I_A}\right) - \left(\frac{1-R}{L}\right). \quad (10)$$

Note that Eqs. (9) and (10) are insensitive to lamp intensity fluctuations since both I and ΔI_A scale proportionately to changes in I_0.

Equation (10) was applied to determine ϵ_B at 687.3 nm by using the change in the transmitted intensity of the O_2 B-band between measurements with synthetic air and an aerosol loaded chamber. As with water vapor absorption, deviations from the Beer–Lambert law must be taken into account with the O_2 absorption. An empirical value of α_{O_2} according to the instrument's resolution was obtained in clean chamber air by interpolating the baseline under the O_2 B-band and using Eq. (1). During the experiment, the value of I_B at the center of the B-band was estimated from the intensity at 683.9 nm (outside the O_2 B-band). A scaling factor was calculated from the transmission spectrum in a clean chamber by interpolating a baseline under the B-band and taking the ratio of the interpolated baseline intensity at 687.3 nm to the intensity at 683.9 nm. For each spectrum, the measured intensity at 683.9 nm was first increased to compensate for H_2O and O_3 absorption. The new reference intensity was then multiplied by the scaling factor to estimate the transmission intensity at 687.3 nm in the absence of H_2O and O_3 absorption. I_B was then calculated by removing the absorption of H_2O and O_3 at 687.3 nm and used in Eq. (10) to retrieve the aerosol extinction.

The background extinction on 15 June retrieved with this procedure is shown in Fig. 6. The precision of the measurements, estimated at the start of the experiment, was $\sim 0.5 \times 10^{-8}\,\text{cm}^{-1}$ (this result can be compared with findings in Ref. [12] at 683 nm for the polluted urban boundary). Aerosol extinction was the major contributor to the background extinction. Figure 6 shows two time periods with significant changes in the background extinction that correlate with the loading of the chamber with aerosol. The background extinction increased from practically $0\,\text{cm}^{-1}$ to $\sim 1 \times 10^{-8}\,\text{cm}^{-1}$ over the period of the first aerosol addition (10:45–11:25 a.m.), which corresponded to an aerosol loading of $5\,\mu\text{g m}^{-3}$. The second, larger increase in ϵ_B coincided with the addition of aerosol from 12:30 to 14:30 p.m. and reached a maximum of $\sim 5.5 \times 10^{-8}\,\text{cm}^{-1}$ when the aerosol concentration reached about $12\,\mu\text{g m}^{-3}$. In both cases, the extinction decreases steadily when aerosol loading stopped and aerosols were deposited on the chamber walls. Other increases in the background extinction were observed around the time (9:00 a.m.) when humidified air was introduced into the chamber and may indicate that the effect of H_2O or O_3 absorption was not completely compensated for in the analysis procedure. Although the above procedure provides a method for retrieving the aerosol extinction based on two intensities, a more comprehensive analysis should use spectral fitting to use more of the O_2 absorption profile.

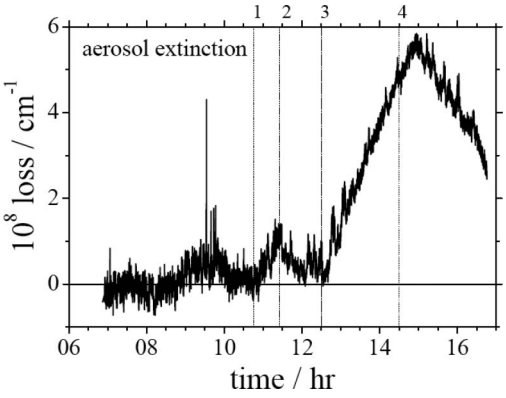

Fig. 6. Background extinction loss at 687 nm on 15 June 2007, retrieved by the procedure outlined in the text. 1, addition of $(NH_4)_2SO_4$ aerosol started (10:45); 2, addition of aerosol ended ($5\,\mu\text{g m}^{-3}$) (11:25); 3, addition of $(NH_4)_2SO_4$ aerosol started (12:30); 4, addition of aerosol ended ($12\,\mu\text{g m}^{-3}$) (14:30).

5. Field Trial at Roches Point

In addition to the chamber experiments, field measurements were taken with a slightly modified instrument at Roches Point, Ireland (51.795 N, 8.252 W) between 29 November and 11 December 2007. Roches Point is the shipping entrance to Cork harbor and is approximately 20 km southeast of Cork city. The transmitter and receiver units were installed on the roof (~43 m above mean sea level) of the Met Éireann weather station (see Fig. 7); electric power, lamp cooling water, and N_2 purge gas were supplied from inside the building. Each unit was mounted on four lead blocks for stability; windbreaker netting tied to the roof railing shielded the units from high winds, and PVC sheet covers protected them from rain. The cavity mirrors (10 m

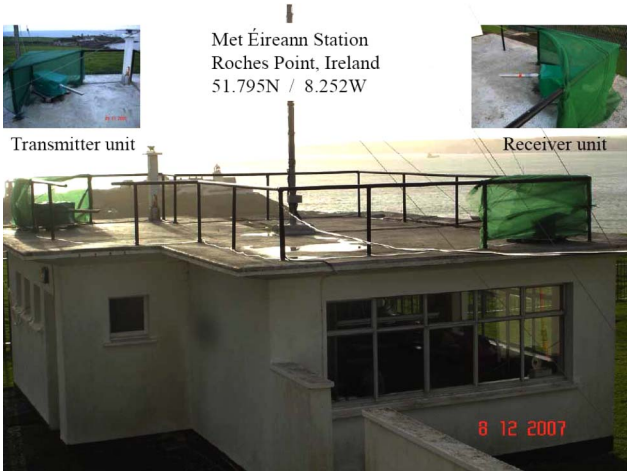

Fig. 7. (Color online) Photograph of the open-path IBBCEA setup on the roof of the Met Éireann weather station at Roches Point (Ireland). The transmitter and receiver units are also shown as insets. The effective cavity length was 6.7 m. The instrument was in this field trial between 29 November and 11 December 2007.

radius of curvature and $R = 0.9998$ at 662 nm) were separated by $l = 8.6$ m, the path length through the open atmosphere was $L \approx 6.7$ m. Spectra were collected with an acquisition time of 1 min. In order to measure I_0 transmission spectra the transmitter and receiver units were connected with a PVC pipe of 10 cm diameter along the optical axis, which was purged with N_2 at a high flow rate. After the initial alignment of the cavity, the pipe for the He–Ne beam was removed and the openings sealed with opaque material to prevent stray light or water from entering the units.

Field observations coincided with a period of high winds and heavy rain, which were unfavorable for open-path measurements. Nevertheless, intermittent spells of calmer weather allowed a few measurements to be made with good sensitivity. The instrument was remarkably stable despite the high winds experienced. Figure 8 shows typical transmission spectra $I_0(\lambda)$ (upper trace) and $I(\lambda)$ (lower trace). The transmission spectrum through the open atmosphere clearly shows the absorption features of O_2 and H_2O in that region. The large decrease in the background is caused by the scattering and absorption of aerosols in the beam path, which often exceeded 10^{-6} cm^{-1}, comparable to highly polluted urban extinction levels [54]. Such high aerosol extinction, which is not surprising given the proximity of the site to the coastline, can have a marked impact on the sensitivity of the instrument. The effective path length of the instrument is <33.5 km at 665 nm in an aerosol-free atmosphere but decreases to <7.7 km when extinction from aerosols corresponds to 10^{-6} cm^{-1}. Assuming an aerosol extinction of 10^{-6} cm^{-1}, an NO_3 detection limit of ~1 pptv for a 1 min integration time was estimated based on the chamber performance. NO_3 was, however, not observed above this limit during the few nighttime periods without rain or mist when meaningful measurements were possible. Such low NO_3 conditions have been observed in marine air masses by other workers [55], who also proposed that NO emissions over land could deplete NO_3 concentrations.

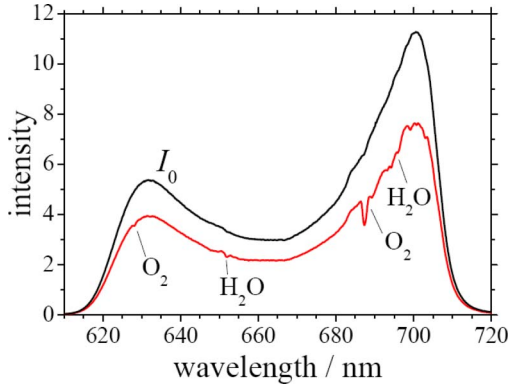

Fig. 8. (Color online) Typical cavity transmission spectra (in units of 10^4 counts) measured at Roches Point (Ireland) on 10 December 2007. Despite fair weather conditions on this day there was no evidence for NO_3 absorption above the detection limit. This figure demonstrates the stability of the system in the field [compare with Figs. 2(a) and 4(a). Lower trace: open-path measurement. Black line: I_0 measurement with a long PVC tube between transmitter and receiver unit that was continuously purged with dry N_2.

6. Summary

A new IBBCEA instrument employing a 20 m optical cavity was utilized in an intercomparison exercise of NO_3 monitoring instruments at the SAPHIR atmosphere simulation chamber at the Forschungszentrum Jülich (Germany) in June 2007. The instrument was designed to detect NO_3 around 662 nm and proved to be robust, experimentally simple, and relatively easy to deploy. The instrument's performance was presented within the context of an aerosol-loaded chamber ($(NH_4)_2SO_4$) under humid conditions (15 June 2007). The concentrations of NO_3 and NO_2, together with the aerosol extinction, were monitored simultaneously. Detection limits of about 2 pptv for NO_3 and 2 ppbv for NO_2 were established for a 5 s acquisition time. The data analysis procedure used an SVD fitting approach in selected spectral windows for fast analytical retrieval of number densities of NO_3 and NO_2. Difficulties in the data retrieval concerning the effective absorption of water vapor in relevant spectral windows were discussed. A procedure was outlined to extract the aerosol extinction at 687 nm based on changes in the fractional absorption of the O_2 B-band. The retrieved aerosol extinction had a precision of about 0.5×10^{-8} cm^{-1}, with a maximum extinction of 5.5×10^{-8} cm^{-1} after loading the chamber with $(NH_4)_2SO_4$ particles ($12\,\mu$g m^{-3}). The deployment of the instrument in the field (at Roches Point, Ireland) was described and its operational stability briefly outlined.

We gratefully acknowledge financial support for this project from the Irish Environmental Protection Agency (Project: "TRACES" 2005-ET-MS-28-M3), for the development of the IBBCEAS field instrument,

and from the European Commission under the 6th Framework Program *Integrated Infrastructure Initiative*: EUROCHAMP (contract number RII3-CT-2004-505968) and *Global Change and Ecosystems*: ACCENT for funding the NO_3-N_2O_5-Intercomparison Campaign 2007. We are much indebted to the SAPHIR personnel, particularly Theo Brauers, Hans-Peter Dorn, and Rolf Häseler for organizing the intercomparison and for their professional help throughout the campaign, and to Franz Rohrer for providing data on H_2O, NO_x, and O_3 concentrations. We thank John Lucey, Joe Sheehan and Christie Roche (UCC) for their professional technical assistance during this work and Johannes Orphal, who contributed to the convolution of some reference spectra. We thank Met Éireann for giving us access to their weather monitoring station at Roches Point, where our work was facilitated by Stewart Vaughan, Chen Jun, John Wenger, and Ian O'Connor, to whom we are also grateful. Finally, we thank the Institute for Analytical Sciences (ISAS), Berlin, for providing some components of the IBBCEAS instrument.

References

1. K. C. Clemitshaw, "A review of instrumentation and measurement techniques for ground-based and airborne field studies of gas-phase tropospheric chemistry," Crit. Rev. Environ. Sci. Technol. **34**, 1–108 (2004).
2. S. S. Brown, "Absorption spectroscopy in high-finesse cavities for atmospheric studies," Chem. Rev. **103**, 5219–5238 (2003).
3. B. A. Paldus and A. A. Kachanov, "An historical overview of cavity-enhanced methods," Can. J. Phys. **83**, 975–999 (2005).
4. S. S. Brown, H. Stark, and A. R. Ravishankara, "Cavity ring-down spectroscopy for atmospheric trace gas detection: application to the nitrate radical (NO_3)," Appl. Phys. B **75**, 173–182 (2002).
5. S. S. Brown, H. Stark, S. J. Ciciora, R. J. McLaughlin, and A. R. Ravishankara, "Simultaneous *in situ* detection of atmospheric NO_3 and N_2O_5 via cavity ring-down spectroscopy," Rev. Sci. Instrum. **73**, 3291–3301 (2002).
6. A. R. Awtry and J. H. Miller, "Development of a cw-laser-based cavity-ringdown sensor aboard a spacecraft for trace air constituents," Appl. Phys. B **75**, 255–260 (2002).
7. J. D. Ayers, R. L. Apodaca, W. R. Simpson, and D. S. Baer, "Off-axis cavity ringdown spectroscopy: application to atmospheric nitrate radical detection," Appl. Opt. **44**, 7239–7242 (2005).
8. S. S. Brown, H. D. Osthoff, H. Stark, W. P. Dube, T. B. Ryerson, C. Warneke, J. A. DeGouw, A. G. Wollny, D. D. Parrish, F. C. Fehsenfeld, and A. R. Ravishankara, "Aircraft observations of daytime NO_3 and N_2O_5 and their implications for tropospheric chemistry," J. Photochem. Photobiol., A **176**, 270–278 (2005).
9. W. P. Dubé, S. S. Brown, H. D. Osthoff, M. R. Nunley, S. J. Ciciora, M. W. Paris, R. J. McLaughlin, and A. R. Ravishankara, "Aircraft instrument for simultaneous, *in situ* measurement of NO_3 and N_2O_5 via pulsed cavity ring-down spectroscopy," Rev. Sci. Instrum. **77**, 034101 (2006).
10. S. Kassi, M. Chenevier, L. Gianfrani, A. Salhi, Y. Rouillard, A. Ouvrard, and D. Romanini, "Looking into the volcano with a mid-IR DFB diode laser and cavity enhanced absorption spectroscopy," Opt. Express **14**, 11442–11452 (2006).
11. S. S. Brown, W. P. Dubé, H. D. Osthoff, D. E. Wolfe, W. M. Angevine, and A. R. Ravishankara, "High resolution vertical distributions of NO_3 and N_2O_5 through the nocturnal boundary layer," Atmos. Chem. Phys. **7**, 139–149 (2007).
12. T. Baynard, E. R. Lovejoy, A. Pettersson, S. S. Brown, D. Lack, H. Osthoff, P. Massoli, S. Ciciora, W. P. Dube, and A. R. Ravishankara, "Design and application of a pulsed cavity ring-down aerosol extinction spectrometer for field measurements," Aerosol Sci. Technol. **41**, 447–462 (2007).
13. T. Nakayama, T. Ide, F. Taketani, M. Kawai, K. Takahashi, and Y. Matsumi, "Nighttime measurements of ambient N_2O_5, NO_2, NO and O_3 in a sub-urban area, Toyokawa, Japan," Atmos. Environ. **42**, 1995–2006 (2008).
14. M. Bitter, S. M. Ball, I. M. Povey, and R. L. Jones, "A broadband cavity ringdown spectrometer for *in situ* measurements of atmospheric trace gases," Atmos. Chem. Phys. **5**, 2547–2560 (2005).
15. R. Wada, J. M. Beames, and A. J. Orr-Ewing, "Measurement of IO radical concentrations in the marine boundary layer using a cavity ring-down spectrometer," J. Atmos. Chem. **58**, 69–87 (2007).
16. H. Fuchs, W. P. Dubé, S. J. Ciciora, and S. S. Brown, "Determination of inlet transmission and conversion efficiencies for *in situ* measurements of the nocturnal nitrogen oxides, NO_3, N_2O_5 and NO_2, via pulsed cavity ring-down spectroscopy," Anal. Chem. **80**, 6010–6017 (2008).
17. S. S. Brown, H. Stark, T. B. Ryerson, E. J. Williams, D. K. Nicks, Jr., M. Trainer, F. C. Fehsenfeld, and A. R. Ravishankara, "Nitrogen oxides in the nocturnal boundary layer: Simultaneous *in situ* measurements of NO_3, N_2O_5, NO_2, NO, and O_3," J. Geophys. Res. **108**(D9), 4299 (2003).
18. S. S. Brown, H. Stark, and A. R. Ravishankara, "Applicability of the steady state approximation to the interpretation of atmospheric observations of NO_3 and N_2O_5," J. Geophys. Res. **108**(D17), 4539 (2003).
19. J. U. White, "Long optical paths of large aperture," J. Opt. Soc. Am. **32**, 285–288 (1942).
20. D. R. Herriott and H. J. Schulte, "Folded optical delay lines," Appl. Opt. **4**, 883–889 (1965).
21. U. Platt, "Modern methods of the measurement of atmospheric trace gases," Phys. Chem. Chem. Phys. **1**, 5409–5415 (1999).
22. J. J. Scherer, "Ringdown spectral photography," Chem. Phys. Lett. **292**, 143–153 (1998).
23. E. R. Crosson, P. Haar, G. A. Marcus, H. A. Schwettman, B. A. Paldus, T. G. Spence, and R. N. Zare, "Pulse-stacked cavity ring-down spectroscopy," Rev. Sci. Instrum. **70**, 4–10 (1999).
24. A. Czyżewski, S. Chudzyński, K. Ernst, G. Karasiński, Ł. Kilianek, A. Pietruczuk, W. Skubiszak, T. Stacewicz, K. Stelmaszczyk, B. Koch, and P. Rairoux, "Cavity ring-down spectrography," Opt. Commun. **191**, 271–275 (2001).
25. S. M. Ball, I. M. Povey, E. G. Norton, and R. L. Jones, "Broadband cavity ringdown spectroscopy of the NO_3 radical," Chem. Phys. Lett. **342**, 113–120 (2001).
26. S. M. Ball and R. L. Jones, "Broad-band cavity ring-down spectroscopy," Chem. Rev. **103**, 5239–5262 (2003).
27. A. A. Ruth, J. Orphal, and S. E. Fiedler, "Fourier-transform cavity-enhanced absorption spectroscopy using an incoherent broadband light source," Appl. Opt. **46**, 3611–3616 (2007).
28. E. Hamers, D. Schram, and R. Engeln, "Fourier transform phase shift cavity ring down spectroscopy," Chem. Phys. Lett. **365**, 237–243 (2002).
29. T. Gherman and D. Romanini, "Mode-locked cavity-enhanced absorption spectroscopy," Opt. Express **10**, 1033–1042 (2002).
30. M. J. Thorpe, K. D. Moll, R. J. Jones, B. Safdi, and J. Ye, "Broadband cavity ringdown spectroscopy for sensitive and rapid molecular detection," Science **311**, 1595–1599 (2006).
31. J. M. Langridge, S. M. Ball, and R. L. Jones, "A compact broadband cavity enhanced absorption spectrometer for detection of atmospheric NO_2," Analyst (Amsterdam) **131**, 916–922 (2006).

32. S. E. Fiedler, A. Hese, and A. A. Ruth, "Incoherent broadband cavity-enhanced absorption spectroscopy," Chem. Phys. Lett. **371**, 284–294 (2003).
33. D. S. Venables, T. Gherman, J. Orphal, J. Wenger, and A. A. Ruth, "High sensitivity *in situ* monitoring of NO_3 in an atmospheric simulation chamber using incoherent broadband cavity-enhanced absorption spectroscopy," Environ. Sci. Technol. **40**, 6758–6763 (2006).
34. T. Gherman, D. S. Venables, S. Vaughan, J. Orphal, and A. A. Ruth, "Incoherent broadband cavity enhanced absorption spectroscopy in the near-ultaviolet: application to HONO and NO_2," Environ. Sci. Technol. **42**, 890–895 (2008).
35. S. Vaughan, T. Gherman, A. A. Ruth, and J. Orphal, "Incoherent broadband cavity-enhanced absorption spectroscopy of the marine boundary layer species I_2, IO and OIO," Phys. Chem. Chem. Phys. **10**, 4471–4477 (2008).
36. S. M. Ball, J. M. Langridge, and R. M. Jones, "Broadband cavity enhanced absorption spectroscopy using light emitting diodes," Chem. Phys. Lett. **398**, 68–74 (2004).
37. M. Triki, P. Cermak, G. Méjean, and D. Romanini, "Cavity-enhanced absorption spectroscopy with a red LED source for NO_x trace analysis," Appl. Phys. B **91**, 195–201 (2008).
38. J. M. Langridge, T. Laurila, R. S. Watt, R. L. Jones, C. F. Kaminski, and J. Hult, "Cavity-enhanced absorption spectroscopy of multiple trace gas species using a supercontinuum radiation source," Opt. Express **16**, 10178–10188 (2008).
39. H.-P. Dorn, R. L. Apodaca, S. M. Ball, T. Brauers, S. S. Brown, R. C. Cohen, J. Crowley, W. P. Dube, J. Fry, H. Fuchs, R. Häseler, U. Heitmann, S. Kato, Y. Kajii, I. Labazan, J. Langridge, J. Matsumoto, J. Meinen, S. Nishida, U. Platt, D. Rollins, A. A. Ruth, E. Schlosser, G. Schuster, A. Shillings, W. Simpson, J. Thieser, R. M. Varma, D. S. Venables, A. Wahner, and P. Wooldridge, "Intercomparison of NO_3 radical detection techniques in the atmosphere simulation chamber SAPHIR," Atmos. Chem. Phys. Discuss. (2008), in preparation.
40. B. Welz, H. Becker-Ross, S. Florek, and U. Heitmann, *High-Resolution Continuum Source AAS: The Better Way to Do Atomic Absorption Spectrometry* (Wiley VCH, 2005).
41. J. Bossmeyer, T. Brauers, C. Richter, F. Rohrer, R. Wegener, and A. Wahner, "Simulation chamber studies on the NO_3 chemistry of atmospheric aldehydes," Geophys. Res. Lett. **33**, L18810 (2006).
42. T. Brauers, J. Bossmeyer, H.-P. Dorn, E. Schlosser, R. Tillmann, R. Wegener, and A. Wahner, "Investigation of the formaldehyde differential absorption cross section at high and low spectral resolution in the simulation chamber SAPHIR," Atmos. Chem. Phys. **7**, 3579–3586 (2007).
43. S. G. Kraus, "DOASIS—A framework design for DOAS," Ph.D. thesis (University of Mannheim, 2006).
44. R. J. Yokelson, J. B. Burkholder, R. W. Fox, R. K. Talukdar, and A. R. Ravishankara, "Temperature dependence of the NO_3 absorption spectrum," J. Phys. Chem. **98**, 13144–13150 (1994).
45. S. Voigt, J. P. Orphal, and J. P. Burrows, "The temperature and pressure dependence of the absorption cross sections of NO_2 in the 250–800 nm region measured by Fourier-transform spectroscopy," J. Photochem. Photobiol. A **149**, 1–7 (2002).
46. L. S. Rothman, D. Jacquemart, A. Barbe, D. C. Benner, M. Birk, L. R. Brown, M. R. Carleer, C. Chackerian Jr., K. V. Chance, V. Dana, V. M. Devi, J.-M. Flaud, R. R. Gamache, A. Goldman, J.-M. Hartmann, K. W. Jucks, A. G. Maki, J.-Y. Mandin, S. Massie, J. Orphal, A. Perrin, C. P. Rinsland, M. A. H. Smith, R. A. Toth, J. Vander Auwera, P. Varanasi, and G. Wagner, "The HITRAN 2004 molecular spectroscopic database," J. Quant. Spectrosc. Radiat. Transfer **96**, 139–204 (2005).
47. F. Rohrer, D. Brüning, E. S. Grobler, M. Weber, D. H. Ehhalt, R. Neubert, W. Schübler, and L. Levin, "Mixing ratios and photostationary state of NO and NO_2 observed during the POPCORN field campaign at a rural site in Germany," J. Atmos. Chem. **31**, 119–137 (1998).
48. J. Orphal, C. E. Fellows, and P. M. Flaud, "The visible absorption spectrum of NO_3 measured by high-resolution Fourier transform spectroscopy," J. Geophys. Res. **108**(D3), 4077–4087 (2003).
49. J. P. Burrows, A. Dehn, B. Deters, S. Himmelmann, A. Richter, S. Voigt, and J. Orphal, "Atmospheric remote-sensing reference data from GOME: 1. Temperature-dependent absorption cross-sections of NO_2 in the 231–794 nm range," J. Quant. Spectrosc. Radiat. Trans. **60**, 1025–1031 (1998).
50. W. H. Press, T. S. Flannery, and W. T. Vetterling, *Numerical Recipes: The Art of Scientific Computing* (Cambridge U. Press, 1986), pp. 51 and 670.
51. H. Fuchs, R. L. Apodaca, S. M. Ball, T. Brauers, S. S. Brown, R. C. Cohen, J. Crowley, H.-P. Dorn, W. P. Dube, J. Fry, R. Häseler, U. Heitmann, S. Kato, Y. Kajii, A. Kiendler-Scharr, I. Labazan, J. Matsumoto, J. Meinen, S. Nishida, U. Platt, F. Rohrer, A. A. Ruth, E. Schlosser, G. Schuster, A. Shillings, W. Simpson, J. Thieser, R. Tillmann, R. M. Varma, D. S. Venables, R. Wegener, and P. Wooldridge, "Intercomparison of different NO_2 measurement techniques at the simulation chamber SAPHIR," Atmos. Chem. Phys. Discuss., in preparation.
52. R. A. Washenfelder, A. O. Langford, H. Fuchs, and S. S. Brown, "Measurement of glyoxal using an incoherent broadband cavity enhanced absorption spectrometer," Atmos. Chem. Phys. Discuss. **8**, 16517–16553 (2008).
53. G. Schuster, I. Labazan, and J. N. Crowley, "A cavity ring down/cavity enhanced absorption device for measurement of ambient NO_3 and N_2O_5," Atmos. Meas. Tech. Discuss. **1**, 67–102 (2008).
54. H. Moosmüller, R. Varma, and W. P. Arnott, "Cavity ring-down and cavity-enhanced detection techniques for the measurement of aerosol extinction," Aerosol Sci. Technol. **39**, 30–39 (2005).
55. R. Sommariva, M. J. Pilling, W. J. Bloss, D. E. Heard, J. D. Lee, Z. L. Fleming, P. S. Monks, J. M. C. Plane, A. Saiz-Lopez, S. M. Ball, M. Bitter, R. L. Jones, N. Brough, S. A. Penkett, J. R. Hopkins, A. C. Lewis, and K. A. Read, "Night-time radical chemistry during the NAMBLEX campaign," Atmos. Chem. Phys. **7**, 587–598 (2007).